

## Distortionless Pulse Transmission in Valley Photonic Crystal Slab Waveguide

Fu-Long Shi,<sup>1,†</sup> Yuan Cao,<sup>2,‡</sup> Xiao-Dong Chen<sup>1D</sup>,<sup>1,‡</sup> Jian-Wei Liu,<sup>1</sup> Wen-Jie Chen,<sup>1</sup> Min Chen,<sup>1,3,\*</sup> and Jian-Wen Dong<sup>1D</sup>,<sup>1,†</sup>

<sup>1</sup>*School of Physics & State Key Laboratory of Optoelectronic Materials and Technologies, Sun Yat-sen University, Guangzhou 510275, China*

<sup>2</sup>*Guangdong Provincial Key Laboratory of Optical Fiber Sensing and Communications, Institute of Photonics Technology, Jinan University, Guangzhou 510632, China*

<sup>3</sup>*Department of Physics, College of Science, Shantou University, Shantou 510063, China*

(Received 17 June 2020; revised 8 October 2020; accepted 4 January 2021; published 1 February 2021)

A valley photonic crystal is one type of photonic topological insulator, the realization of which needs only  $P$ -symmetry breaking. The domain wall between two valley-contrasting photonic crystals supports robust edge states, which can wrap around sharp corners without backscattering. Using the robust edge states, one can achieve pulse transmission. Here, using time-domain measurements in the microwave regime, we show distortionless pulse transmission in a sharply bended waveguide. An  $\Omega$ -shaped waveguide with four  $120^\circ$  bends is constructed with the domain wall between two valley photonic crystal slabs. Experimental results show the progress of Gaussian pulse transmission without distortion, and the full width at half maximum of the output signal changes slightly in the  $\Omega$ -shaped waveguide. By measuring the steady-state electric field distribution, we also confirm the confined edge states without out-of-plane radiation, which benefits from dispersion below the light line. Our work provides a way for high-fidelity optical pulse signal transmission and the development of high-performance optical elements, such as photonic circuits or optical delay lines.

DOI: 10.1103/PhysRevApplied.15.024002

### I. INTRODUCTION

Due to the important role that pulse transmission plays in modern optical science, researchers have studied pulse transmission in several photonic structures, such as photonic ridge waveguides [1], photonic crystal waveguides [2–5], photonic crystal fibers [6,7], and surface plasmon polariton waveguides [8–11]. Many optical phenomena, such as slow light [3,8], pulse reshaping [9], and third-harmonic generation [5], are observed by measuring the pulse. Nevertheless, distortionless pulse transmission without scattering, resonance, and frequency dispersion in the waveguide is desirable in high-fidelity optical information transmission and processing.

A photonic crystal, as one type of artificial periodic optical structure, can realize several kinds of light manipulation, such as zero-index focusing [12,13], slow light [14–16], and cloaking [17]. Guiding light is one of the important applications of a photonic crystal [18], which makes it possible to transmit optical information in integrated optoelectronic devices. However, when light

encounters defects, disorders, or sharp bends, obvious backscattering will lead to energy loss and signal distortion. Therefore, distortionless pulse transmission without backscattering in a photonic crystal is desirable. In the last decade, the introduction of topology into the optical systems has inspired the appearance of photonic topological insulators [19–21]. Robust transport of the edge states against defects has been achieved in gyromagnetic photonic crystals [22–24], coupled resonators [25,26], helical photonic waveguides [27], or bianisotropic metacrystals [28]. It means that backscattering can be suppressed in photonic topological insulators, and they are expected to be used in high-fidelity optical information transmission. However, the employment of magnetism, time-domain modulations, or complicated designs of metamaterials bring difficulties in miniaturization for application in the communication regime. Recently, a type of photonic topological insulator, i.e., a valley photonic crystal (VPC), has been well explored and several devices have been demonstrated [29–36]. As broken inversion symmetry is required, it can be applied within all-dielectric structures [29,34–36] and has the potential to be used in integrated optoelectronic devices [35,36]. The domain wall between two different VPCs can guide light through sharp bends without backscattering. Waveguides constructed from this type of artificial dielectric structure are expected to guide

\*stscm@mail.sysu.edu.cn

†dongjwen@mail.sysu.edu.cn

‡F.-L. Shi, Y. Cao, and X.-D. Chen contributed equally to this work.

pulse signals through sharp bends without distortion. The combination of robust transport and pulse signal transmission will be beneficial for the potential application of VPCs in optical communication.

Herein, we design a type of waveguide constructed from VPC slabs with dielectric rods standing on a perfect electric conductor (PEC) substrate. We experimentally measure and analyze in detail the Gaussian pulse, which is guided through an  $\Omega$ -shaped waveguide, to verify the distortionless pulse transmission against sharp bends. Field confinement of the valley-dependent edge states is also observed by measuring steady-state electric field distributions.

## II. DESIGN OF A WAVEGUIDE FOR DISTORTIONLESS PULSE TRANSMISSION

Distortionless transmission is a desirable feature to avoid intersymbol interference in the information channel and becomes the key to guarantee the transmission bandwidth in optical communication. For a linear time-invariant system, it naturally means that different frequency components should propagate in the information channel without phase distortion and amplitude distortion, i.e., these components arrive at the same time with the same gain. This simultaneity requires that different frequency components should propagate with the same group velocity, which is estimated by the group-velocity dispersion (GVD) of the channel. The same gain requires that different frequency components should suffer energy losses (scattering loss, radiation loss, absorption loss etc.) at the same rate, preferably no losses. Therefore, one would expect a waveguide channel with a low GVD and low transmission loss.

The VPC slab is an ideal platform to realize low-loss distortionless pulse transmission. The domain wall between two VPCs supports edge states due to their distinct topology. It can serve as an information channel. Since these edge states are derived from the effective Hamiltonian near  $K$  and  $K'$  valleys, the dispersions are typically linear near these  $k$  points. This guarantees a similar group velocity (defined by  $v_g = d\omega/dk$ ). The phase distortions caused by frequency-dependent time delays are thus mild. On the other hand, these topological edge states are robust against backscattering, even when sharp bends exist, so that the in-plane scattering loss can be suppressed. Since the linear edge dispersion can be located below the light line by using appropriate parameters, the out-of-plane radiation loss is suppressed. Therefore, the amplitude distortion due to frequency-dependent loss can be minimized in our system. Additionally, we use a PEC substrate to filter TE-like modes ( $E$  field is mostly parallel to the mirror plane of slabs and is exactly parallel at  $z=0$ ) and leave only the TM-like ( $E$  field is mostly perpendicular to the mirror plane of slabs and is exactly perpendicular at  $z=0$ )

edge states inside the complete band gap [37]. Thus, the loss deriving from cross-coupling between TM-like and TE-like modes is reduced.

The two VPC slabs (VPC1 and VPC2) in our experiment are depicted in Fig. 1(a). Both slabs are composed of ceramic rods ( $\varepsilon_r = 9$ ) arranged in a honeycomb lattice, which is a combination of two triangular sublattices (marked by  $A$  and  $B$ ) with the same lattice constant of  $a = 20$  mm. The heights of all ceramic rods are  $h = 17$  mm. The diameter of rod  $A$  is  $d_A = 7.5$  mm ( $d_A = 5.6$  mm), while the diameter of rod  $B$  is  $d_B = 5.6$  mm ( $d_B = 7.5$  mm) for VPC1 (VPC2). VPC2 is the inversion partner of VPC1. Both slabs stand on an aluminum plate (assumed to be PEC in the microwave regime). Figure 1(a) shows the TM-like bulk bands of two slabs, where VPC1 and VPC2 share a common complete band gap, but their topologies are different due to the opposite valley Chern number  $C_V = C_K - C_{K'}$  [35]. To see this, we calculate the Berry curvature of both VPC slabs [Fig. 1(c)]. As shown in the left panel of Fig. 1(c), the Berry curvature of the first bulk band of VPC1 is positive and concentrated around the  $K$  point in the momentum space (Berry curvature around the  $K'$  point is opposite to that around the  $K$  point due to time reversal symmetry). On the contrary, the Berry curvature of VPC2 is negative and concentrated around the  $K$  point [right panel of Fig. 1(c)]. These opposite Berry curvature distributions between VPC1 and VPC2 show different topologies and indicate the valley-projected edge states. Notably, as bulk bands of VPC slab are not well described by the Dirac equation; it leads to a deviation of the numerical valley Chern numbers from  $\pm 1$ . Detailed numerical Berry curvatures and valley Chern numbers are investigated in Appendix A.

According to the bulk-edge correspondence, the domain wall between VPC1 and VPC2 [sketch in Fig. 1(b)] supports edge states and enables robust transport along the  $\Gamma K - \Gamma K'$  direction due to the suppression of intervalley scattering [35]. Figure 1(d) calculates the edge dispersion of the domain wall, where the green line highlights the edge states and the gray area covers the light cone. The experimental edge dispersion (obtained by Fourier transformation of the measured  $E_z$  fields) labeled with bright spots fits well with the simulated band curve. The frequency of the edge states below the light line ranges from 5.67 to 5.92 GHz, where the out-of-plane radiation should be neglectable. The calculated group velocity (defined as  $v_g = \partial\omega/\partial k_x$ ) and GVD [defined as  $D = (\omega^2/2\pi c)(1/v_g^3)(\partial v_g/\partial k_x)$ ] of the edge dispersion are shown in Figs. 1(e) and 1(f), respectively. The nearly constant group velocity (near-zero GVD) around 5.88 GHz (marked by black dashed lines) shows a good linearity of edge dispersion and guarantees the suppression of phase distortion. Therefore, we choose 5.88 GHz as the central frequency of the input Gaussian pulse in the experiments. The full bandwidth at half maximum (FBHM) of the pulse

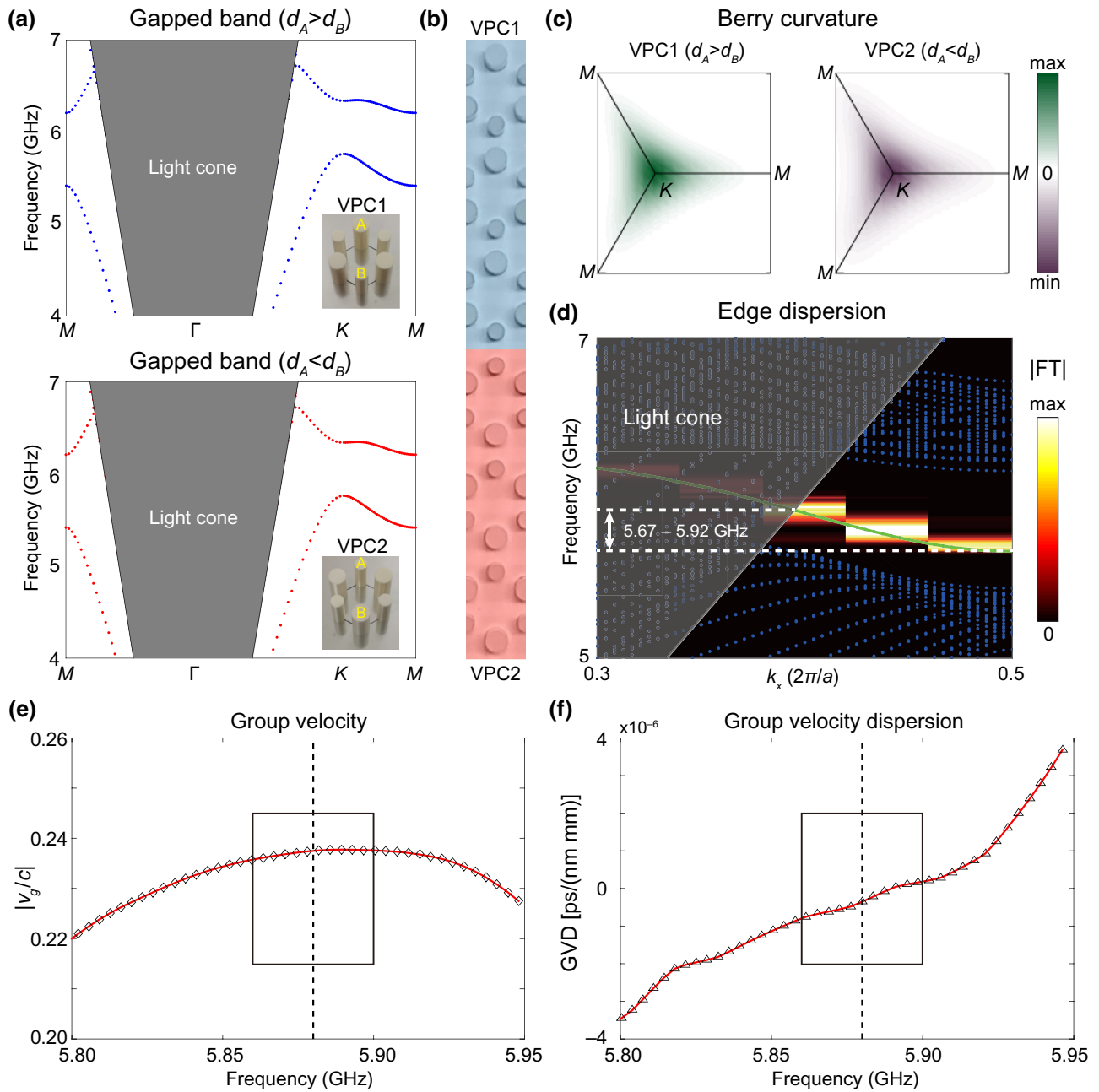


FIG. 1. Group velocity ( $v_g$ ) and GVD of edge states. (a) Gapped bulk bands of two VPC slabs with the honeycomb lattice on a PEC substrate (top, VPC1 with  $d_A > d_B$ ; bottom, VPC2 with  $d_A < d_B$ ). Two slabs share the same bulk band gap. (b) Domain wall between two slabs. (c) Berry curvature of VPC1 and VPC2. (d) Edge dispersion of the domain wall in (b). Shaded area is the light cone. Green solid curve corresponds to the simulated edge dispersion; bright spots plot experimental results. (e) Calculated group velocity ( $v_g$ ) and (f) GVD of edge states, which exhibit a uniform pulse velocity at frequencies around 5.88 GHz. This guarantees the distortionless transmission of the Gaussian pulse.

is set to be 40 MHz, i.e., frequency range 5.86–5.90 GHz (marked by the black boxes).

### III. EXPERIMENTAL DEMONSTRATION OF DISTORTIONLESS PULSE TRANSMISSION

In our experiments, pulse transmission through the waveguides will be studied in detail to confirm the

distortionless pulse transmission. We employ an arbitrary waveform generator (Tektronix AWG70002A) to generate the Gaussian pulse. The input signal is launched into the waveguides from the entrance (i.e., the leftmost end of the channel) through a dipole antenna along the  $z$  direction, and the  $E_z$  field signal inside the waveguide channel is measured by another dipole antenna connected to an oscilloscope (Teledyne LeCroy MCM-Zi, 10-36Zi).

We first study pulse transmission in a straight waveguide [Fig. 2(a)] to assess the phase distortion due to GVD. We monitor the evolution of the pulse waveform throughout the waveguide by measuring the time-domain signals at seven different positions (marked by blue and red stars, every  $5a$  away from the entrance). Due to insertion loss at the entrance, we measure and compare only the signals

inside the waveguide channel. The signal received at the blue star ( $5a$  away from the entrance) is shown in the inset of Fig. 2(a) and has a typical Gaussian shape. Its full width at half maximum (FWHM) is estimated to be 23.52 ns by Gaussian fitting. Without loss of generality, we assume the arrival time at this position of the pulse center to be  $t = 0$  and the distance of the position to be  $d = 0$ . Likewise, the

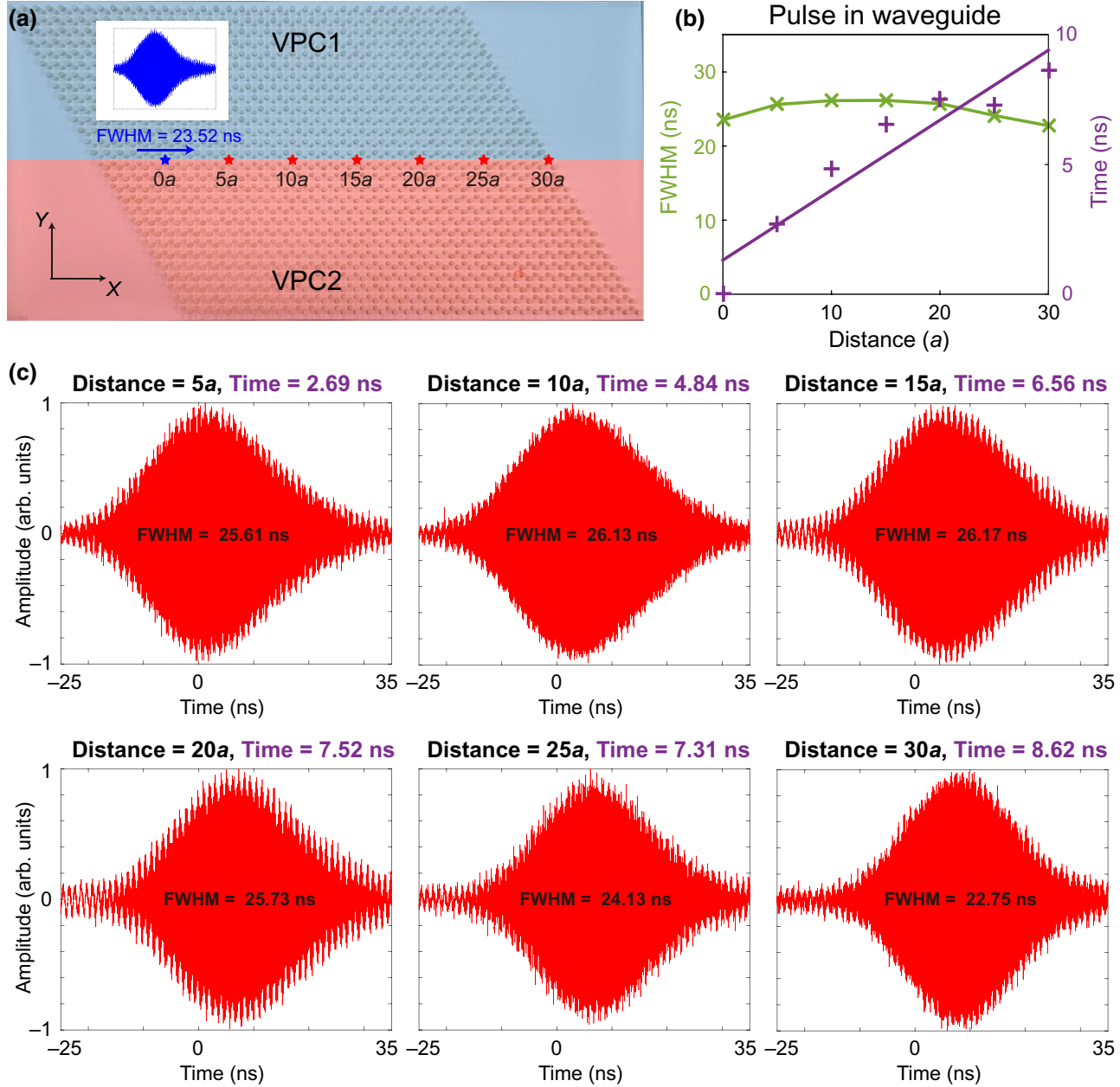


FIG. 2. Distortionless pulse transmission in straight VPC slab waveguide. (a) Photograph of the straight waveguide. It consists of two VPC slabs with opposite topological indices. Blue and red stars mark positions of the detectors. Inset: measured Gaussian pulse, which is centered at 5.88 GHz with a FBHM of 40 MHz. (b) Green cross, FWHM of the measured Gaussian pulse at different distances. FWHM of the pulse at the rightmost exit changes only 3.27% compared with that of the input pulse. Purple cross, arrival time of the pulse center as a function of distance. Purple line, linear fitting relationship between arrival time and distance, indicating that the averaged group velocity of the pulse throughout the waveguide is  $\bar{v}_g = 0.247c$ . (c) Measured pulse at different distances [marked by red stars in (a)] in the straight waveguide.

time-domain signals recorded at other positions (separately normalized by the maximum amplitude of themselves) are plotted in Fig. 2(c). We see that the pulse signals maintain a Gaussian shape during transmission and no obvious deformation occurs. Their FWHMs (25.61, 26.13, 26.17, 25.73, 24.13, and 22.75 ns) and the arrival times of the pulse center (2.69, 4.84, 6.56, 7.52, 7.31, and 8.62 ns) are obtained by performing Gaussian fitting, as depicted in Fig. 2(c). We summarize the arrival times and FWHMs as a function of distance in Fig. 2(b). The arrival times have a relatively linear dependence on the distance, which means that the wave packet propagates with almost a constant speed. From Fig. 2(b), it seems that the pulse arrives at the last two points ( $25a$ ,  $30a$ ) in advance and earlier than the other points. This is because our measured signals are the superpositions of the forward pulse and the backward pulse reflected by the exit interface. The reflected waves will affect the fitting pulse center. The averaged group velocity of the pulse center throughout the waveguide channel is estimated to be  $\bar{v}_g = 0.247c$  using linear fitting [see the purple line in Fig. 2(b)], which agrees well with the theoretical prediction [ $v_g = 0.238c$ , obtained in Fig. 1(d)]. On the other hand, the FWHMs recorded at different positions are almost the same, with about 11.27% variation throughout the waveguide channel, due to the similar group velocities of the different frequency components guaranteed by the linear edge dispersion. The slight variation may be due to the superpositions of the forward pulse and the reflected pulse. Specifically, the FWHM of the pulse at the exit (the right-most end of the channel,  $d = 30a$ ) is 22.75 ns (only 3.27% deviated from the signal at  $d = 0$ ), indicating little phase distortion.

Other than GVD, other frequency-dependent responses would also lead to waveform distortion, such as frequency-dependent scattering loss or frequency-dependent time delay caused by defects. Therefore, we further study an  $\Omega$ -shaped waveguide with four  $120^\circ$  bends [Fig. 3(a)] and measure pulse transmission to assess waveform distortion. Theoretically, the amplitude distortion caused by frequency-dependent scattering loss can be suppressed by the backscattering immunity of topological edge states. Although these edge states would eventually wrap around the corner after a while, time delays for different frequency components are generally different. This may result in phase distortion and will be studied in our experiment.

Similar to the straight waveguide, we monitor the waveform evolution at 12 different positions (marked by blue and red stars,  $5a$ ,  $10a$ ,  $15a$ , ...,  $50a$ ,  $55a$ , and  $59a$  away from the entrance along the channel). The signal received at the blue star ( $5a$  away from the entrance) is shown in the inset of Fig. 3(a) and has a typical Gaussian shape. Its FWHM is estimated to be 22.03 ns by Gaussian fitting. The arrival time of the pulse center and the distance of the position are assumed to be zero. Likewise, the time-domain signals recorded at other positions (separately

normalized by the maximum amplitude of themselves) are plotted in Fig. 3(c). The pulse signals maintain a Gaussian shape and no obvious deformation occurs, even after going through four  $120^\circ$  sharp bends. This reflects that the frequency dependency of time delays is not obvious in our system. Their FWHMs (22.04, 21.05, 21.64, 22.33, 20.91, 21.42, 23.66, 24.96, 21.04, 22.11, and 21.00 ns) and the arrival times of pulse center (1.34, 3.31, 6.02, 7.46, 9.02, 10.87, 13.32, 15.04, 14.69, 16.73, and 18.17 ns) are depicted in Fig. 3(c). We summarize the arrival times and FWHMs as a function of distance in Fig. 3(b). The relatively linear dependence of arrival times on the distance shows an almost constant speed of the wave packet. The pulse arrives at the last three points ( $45a$ ,  $50a$ ,  $54a$ ) in advance due to the backward pulse being reflected by the exit interface. The averaged group velocity of the pulse center throughout the waveguide channel is estimated to be  $\bar{v}_g = 0.196c$  [see the purple line in Fig. 3(b)], which is 17.65% smaller than that of the theoretical prediction [ $v_g = 0.238c$ , as obtained in Fig. 1(d)]. This lower averaged group velocity is caused by time delays at the corners. Although backscattering is suppressed, the pulse signal is delayed at the corners, so that the averaged group velocity will be reduced. On the other hand, the FWHMs recorded at different positions are almost the same, with only about 13.30% variation throughout the waveguide channel. The slight variation may be due to superpositions of the forward pulse and the reflected backward pulse. Specifically, the FWHM of the pulse at the exit (the right-most end of the channel,  $d = 54a$ ) is 21.00 ns (only 4.68% deviation from the signal at  $d = 0a$ ), indicating that time delays of different frequency components at the corners are almost the same. The distortionless pulse transmission in the  $\Omega$ -shaped waveguide benefits not only from little phase distortion (guaranteed by the low GVD and nearly frequency-independent time delay at the corners), but also from little amplitude distortion (guaranteed by the topologically protected edge state).

Notably, the total propagation times of the pulse are different in the two waveguides. Although they have the same sample sizes (the lengths along  $x$  direction are both  $35a$ ), the optical distances of the two waveguides are different ( $35a$  in the straight waveguide and  $59a$  in the  $\Omega$ -shaped waveguide). Due to the different optical distances and time delays at the corners, the propagation time in the  $\Omega$ -shaped waveguide (18.17 ns) is longer than that in the straight waveguide (8.62 ns). This provides a way to design an on-chip robust optical delay line [25] with VPC slabs. The feature of a nearly frequency-independent time delay of this delay line is useful for pulse signal transmission. In the experimental demonstration, we consider only the dispersionless part of the edge states below the light line to avoid propagation loss and pulse distortion. As a result, the frequency bandwidth of the pulse used is only 4.3%, and it leads to the long Gaussian signal used. Thus, the

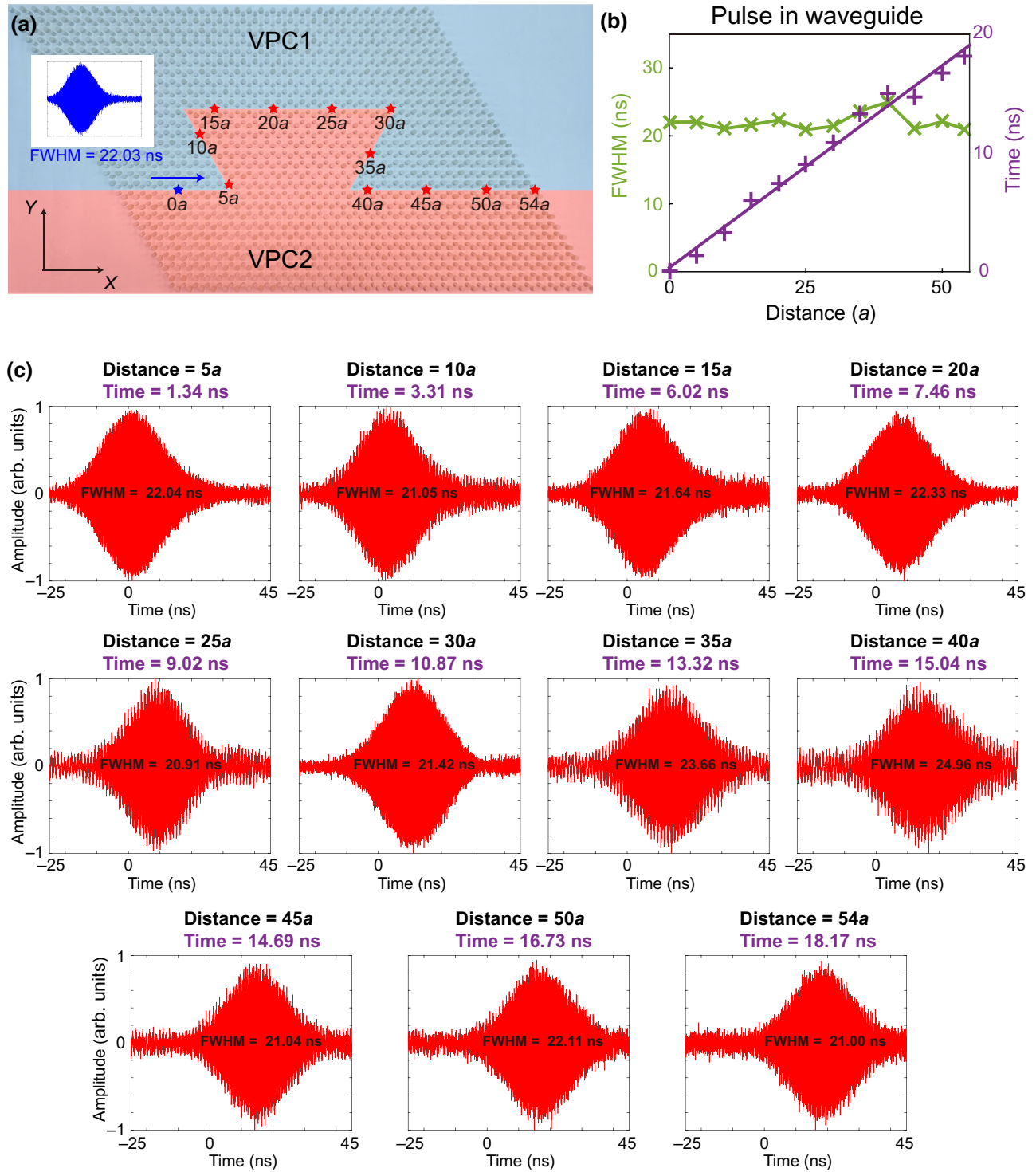


FIG. 3. Distortionless pulse transmission in an  $\Omega$ -shaped VPC slab waveguide. (a) Photograph of the  $\Omega$ -shaped waveguide. Blue and red stars indicate positions of the detectors. Inset: measured Gaussian pulse (centered around 5.88 GHz, FBHM = 40 MHz) at the blue star. (b) Green cross, FWHM of the measured Gaussian pulse at different distances. FWHM of the pulse at the rightmost exit changes only 4.68% compared with the input pulse. Purple cross, the arrival time of the pulse center as a function of distance. Purple line, linear fitting of the arrival time, indicating that the averaged group velocity of the pulse throughout the waveguide is  $\bar{v}_g = 0.196c$ . (c) Measured pulse at different distances [marked by red stars in (a)] in the  $\Omega$ -shaped waveguide.

frequency bandwidth of pulse transmission is narrower than that of a conventional photonic crystal waveguide (approximately 20% frequency bandwidth) and that of a conventional silicon strip waveguide (>30% frequency bandwidth). To broaden the frequency bandwidth (i.e., a shorter time duration) for pulse transmission, one can optimize the structural parameters of the VPC waveguide by boundary decoration (e.g., adjusting the position or radii of the rods nearest to the boundary). In Appendix B, we develop a method to increase the frequency bandwidth for pulse transmission and successfully increase the frequency bandwidth from 4.3% to 7.9%. It is important to note that, although the frequency bandwidth in the VPC waveguide is not so broadband, pulse transmission is robust against sharp bends, which is hard to realize in a conventional waveguide.

#### IV. FIELD CONFINEMENT OF EDGE STATES

In previous sections, distortionless pulse transmissions in VPC slab waveguides are studied in the time domain. In this part, we discuss field confinement of the edge state by measuring the steady-state electric field distributions of the waveguides. A vector network analyzer (VNA, Keysight E5071C) is used to generate an input source and measure the field distribution. A dipole antenna connected to the VNA is used to excite the TM-like edge states, and another dipole antenna fixed on a motor scanning platform is used to receive the electric field,  $E_z$ . We study the in-plane ( $x$ - $y$  plane) field confinement first. We measure the steady-state

$E_z$  field distributions 1 mm above the straight and  $\Omega$ -shaped waveguides; the measured amplitudes at 5.88 GHz (center of the Gaussian pulse) are shown in Figs. 4(a) and 4(b). Large amplitudes near the channel are observed not only in the straight waveguide, but also in the  $\Omega$ -shaped waveguide. The electromagnetic (EM) wave does not scatter or radiate to the bulk crystal, even when it propagates through four 120° sharp bends, showing good in-plane confinement. This is guaranteed by the backscattering-immune property of VPCs. Furthermore, we study the out-of-plane field confinement of the edge state (in the  $x$ - $z$  plane) in the straight waveguide. We predict that the EM wave in the frequency range of the edge state below the light line (5.67–5.92 GHz) will be confined well in the waveguide in the absence of the propagating mode in air. In Fig. 4(c), we show an  $E_z$  amplitude of 5.88 GHz in the  $x$ - $z$  plane (the cross section along the  $x$  direction in the middle of the straight waveguide). The white dashed line labels the top surface of the photonic crystal slab. The EM wave is concentrated inside the waveguide and decays rapidly upon moving away from the top surface. This shows good out-of-plane confinement. Additionally, we also confirm confinement at different frequencies. For each frequency and  $z$  coordinate, we sum up the measured  $|E_z|$  of all  $x$  positions; the frequency spectrum of out-of-plane field confinement is shown in Fig. 4(d). We find that  $|E_z|$  in the frequency range of 5.67–5.92 GHz is larger and most of the fields are concentrated in the photonic crystal slab. While out of this frequency range, localization of the EM wave becomes weak.

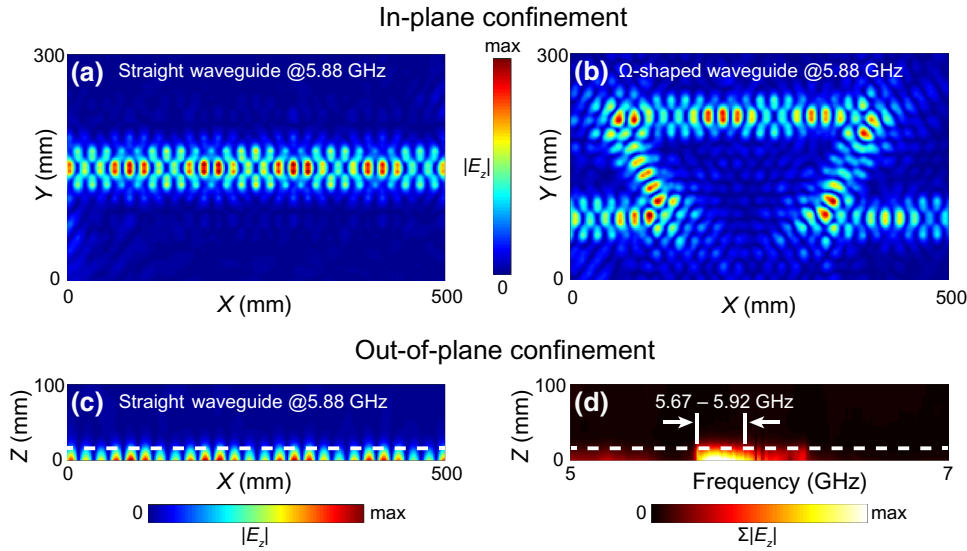


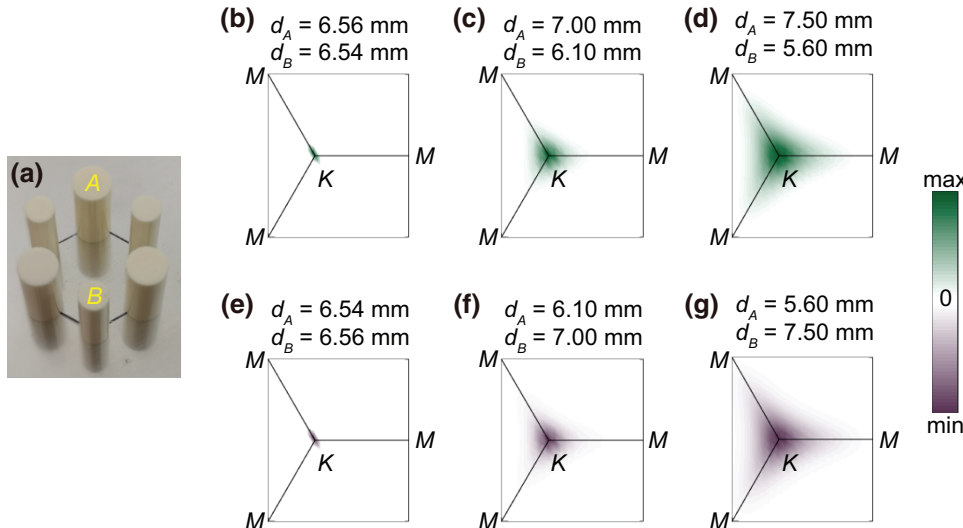
FIG. 4. Field confinement of the measured edge states. In-plane confinement measured for  $E_z$  field distributions of the edge states in (a) straight and (b)  $\Omega$ -shaped waveguides at 5.88 GHz (center of the Gaussian pulse) in the  $x$ - $y$  plane, which confirms good confinement and robust transport of the edge states. (c) Out-of-plane confinement measured for  $E_z$  field distributions in the straight waveguide at 5.88 GHz in the  $x$ - $z$  plane. Out-of-plane distribution shows that the edge states are confined well in the waveguide, but decay rapidly upon moving away from the top surface of the sample (denoted by white dashed line). (d) Out-of-plane field confinement of edge states for different frequencies.

## V. CONCLUSIONS

We design a type of VPC slab waveguide standing on a PEC substrate. The distortionless pulse transmission in the waveguide is predicted by analyzing the linearity of the edge dispersion and the nontrivial band topology of the VPCs. Based on time-domain measurements, we directly observe distortionless Gaussian pulse signals in a straight waveguide and an  $\Omega$ -shaped waveguide. By analyzing these pulse signals, we obtain their FWHMs. The results show a slight variation of the FWHMs. Additionally, using steady-state near-field scan technology, we experimentally confirm the field confinement of edge states in the VPC waveguides. This work gives experimental evidence of distortionless pulse transmission against sharp bends by using linear valley-projected edge states under the light line. It is a combination of robust transport and pulse transmission, which may lead to the potential application of VPCs in optical communication. Time-domain measurements also provide a different method to study the influence of topology on pulse transmission. Taking advantage of a large time delay, the bent VPC waveguide has the potential to be used as a robust optical delay line for pulse signal transmission in integrated photonic circuits.

## ACKNOWLEDGMENTS

This work is supported by the National Natural Science Foundation of China (Grants No. 11874435, No. 11761161002, No. 62035016, and No. 12074443), the Natural Science Foundation of Guangdong Province (Grant No. 2018B030308005), the Guangdong Basic and Applied Basic Research Foundation (Grant No. 2019B151502036), and the Fundamental Research Funds for the Central Universities (Grant No. 20lgzd29).



## APPENDIX A: NUMERICAL BERRY CURVATURE AND VALLEY CHERN NUMBER

Herein, we study the numerical Berry curvature and valley Chern number of VPC slabs with different diameter differences between rods *A* and *B* (Fig. 5). Based on the honeycomb lattice in Fig. 5(a), we gradually tune the difference between the diameters of rods *A* and *B* ( $d_A$  and  $d_B$ ) and study the evolution of Berry curvature around the *K* point and the numerical valley Chern number. In Fig. 5(b), when the diameters of rods *A* and *B* are slightly different ( $d_A = 6.56 \text{ mm}$  and  $d_B = 6.54 \text{ mm}$ ), the Berry curvature is well localized near the *K* point, and the numerical valley Chern number is  $C_V = C_K - C_{K'} = 0.994 \approx 1$ . When the diameter difference becomes larger (e.g.,  $d_A = 7.00 \text{ mm}$  and  $d_B = 6.10 \text{ mm}$ ), the localization of the Berry curvature will become weaker [Fig. 5(c)]. The numerical valley Chern number is 0.709, which is smaller than one. Figure 5(d) shows the case of VPC1 ( $d_A = 7.50 \text{ mm}$  and  $d_B = 5.60 \text{ mm}$ ). The localization of the Berry curvature is further weakened, and the valley Chern number is 0.464, which is much different from one. Notably, the VPCs in Figs. 5(e)–5(g) are the inversion partners of those in Figs. 5(b)–5(d), so their numerical valley Chern numbers are  $-0.994$ ,  $-0.709$ , and  $-0.464$ , respectively, which are the opposite values of the valley Chern numbers of VPCs in Figs. 5(b)–5(d).

As a result, when the diameter difference between the two rods becomes larger, the localization of the Berry curvature will become weaker, and the numerical valley Chern number will increasingly deviate from  $\pm 1$ . This is because the ideal value of  $\pm 1$  is derived from the Dirac equation,  $H = v_D(\hat{\tau}_z\hat{\sigma}_x\delta k_x + \hat{\sigma}_y\delta k_y) + \lambda\hat{\tau}_z\hat{\sigma}_z$ . However, when the diameter difference between the two rods becomes larger, the bulk bands of the VPC are not well described by the Dirac equation, leading to a deviation of the valley Chern numbers from  $\pm 1$ . Although the valley

FIG. 5. Calculated Berry curvatures of VPC slabs of two rods with different diameters. (a) Photograph of the unit cell of VPC slab with honeycomb lattice. (b)–(d) Berry curvatures around the *K* point when  $d_A > d_B$ . (e)–(g) Berry curvatures around the *K* point when  $d_A < d_B$ .

Chern numbers of VPC1 and VPC2 deviate from  $\pm 1$ , the Berry curvatures are opposite to each other and this indicates the valley-projected edge states.

## APPENDIX B: ENLARGING FREQUENCY BANDWIDTH FOR PULSE TRANSMISSION

Herein, we develop a method to increase the frequency bandwidth of edge states for pulse transmission and increase the frequency bandwidth from 4.3% to 7.9%. To increase the frequency bandwidth, we can first reduce the frequencies of the bulk bands, so that they are located below the light cone, then enlarge the band gap, and lastly increase the ratio of edge states inside the band gap. Based on the above ideas, we have the following optimization: first, to reduce the frequencies of bulk bands, we can increase the effective refractive index of the VPC slab by enlarging the refractive index, diameter, or height of all rods. In the concrete example, we increase the relative permittivity of all rods from 9 to 16. Then, to enlarge the band gap, we further increase the diameter difference between rod *A* and rod *B*. In the concrete example, the diameters of rod *A* and rod *B* in VPC1 (VPC2) are changed to  $d_A = 8.00$  mm and  $d_B = 5.10$  mm ( $d_A = 5.10$  mm and  $d_B = 8.00$  mm). Finally, to increase the ratio of the edge states inside the band gap, we can modify the boundary morphology. In the concrete example, we change the diameters of two rods at the middle of the boundary to 6.55 mm [these two rods are named as the transition layer in Fig. 6(a)]. The introduction of this transition layer makes the edge states locate at the middle frequency of the band gap, and it effectively increases the ratio of the edge states inside the band gap. The dispersion of the edge states of the optimized boundary is shown in Fig. 6(b). The frequency bandwidth is increased to 7.9% (4.73–5.12 GHz).

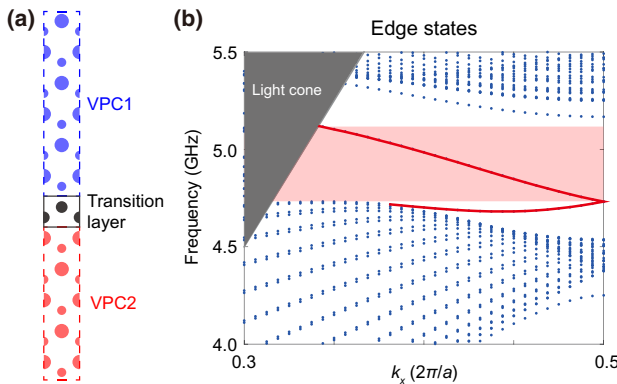


FIG. 6. Design for edge states with larger frequency bandwidth. (a) Domain wall with a transition layer between two VPC slabs. (b) Edge dispersion of the structure in (a). Frequency bandwidth of edge states for pulse transmission is 7.9% (4.73–5.12 GHz).

- [1] M. L. M. Balistreri, H. Gersen, J. P. Korterik, L. Kuipers, and N. F. v. Hulst, Tracking femtosecond laser pulses in space and time, *Science* **294**, 1080 (2001).
- [2] H. Gersen, T. J. Karle, R. J. Engelen, W. Bogaerts, J. P. Korterik, N. F. van Hulst, T. F. Krauss, and L. Kuipers, Real-Space Observation of Ultraslow Light in Photonic Crystal Waveguides, *Phys. Rev. Lett.* **94**, 073903 (2005).
- [3] R. J. P. Engelen, Y. Sugimoto, Y. Watanabe, J. P. Korterik, N. Ikeda, N. F. v. Hulst, K. Asakawa, and L. Kuipers, The effect of higher-order dispersion on slow light propagation in photonic crystal waveguides, *Optics Express* **14**, 1658 (2006).
- [4] R. J. P. Engelen, Y. Sugimoto, H. Gersen, N. Ikeda, K. Asakawa, and L. Kuipers, Ultrafast evolution of photonic eigenstates in  $k$ -space, *Nat. Phys.* **3**, 401 (2007).
- [5] C. Monat, C. Grillet, M. Collins, A. Clark, J. Schroeder, C. Xiong, J. Li, L. O'Faolain, T. F. Krauss, B. J. Eggleton, and D. J. Moss, Integrated optical auto-correlator based on third-harmonic generation in a silicon photonic crystal waveguide, *Nat. Commun.* **5**, 3246 (2014).
- [6] H. Han, H. Park, M. Cho, and J. Kim, Terahertz pulse propagation in a plastic photonic crystal fiber, *Appl. Phys. Lett.* **80**, 2634 (2002).
- [7] W. H. Reeves, D. V. Skryabin, F. Biancalana, J. C. Knight, P. S. J. Russell, F. G. Omenetto, A. Efimov, and A. J. Taylor, Transformation and control of ultrashort pulses in dispersion-engineered photonic crystal fibres, *Nature* **424**, 511 (2003).
- [8] M. Sandtke and L. Kuipers, Slow guided surface plasmons at telecom frequencies, *Nat. Photonics* **1**, 573 (2007).
- [9] Z. L. Sámon, P. Horak, K. F. MacDonald, and N. I. Zheludev, Femtosecond surface plasmon pulse propagation, *Opt. Lett.* **36**, 250 (2011).
- [10] H. M. Su, Z. H. Hang, Z. Marcet, H. B. Chan, C. T. Chan, and K. S. Wong, Propagation dynamics of femtosecond pulse through subwavelength metallic hole arrays, *Phys. Rev. B* **83**, 245449 (2011).
- [11] Z. Gao, H. Xu, F. Gao, Y. Zhang, Y. Luo, and B. Zhang, Surface-Wave Pulse Routing around Sharp Right Angles, *Phys. Rev. Appl.* **9**, 044019 (2018).
- [12] X. Huang, Y. Lai, Z. H. Hang, H. Zheng, and C. T. Chan, Dirac cones induced by accidental degeneracy in photonic crystals and zero-refractive-index materials, *Nat. Mater.* **10**, 582 (2011).
- [13] J. Mei, Y. Wu, C. T. Chan, and Z.-Q. Zhang, First-principles study of Dirac and Dirac-like cones in phononic and photonic crystals, *Phys. Rev. B* **86**, 035141 (2012).
- [14] Y. A. Vlasov, M. O'Boyle, H. F. Hamann, and S. J. McNab, Active control of slow light on a chip with photonic crystal waveguides, *Nature* **438**, 65 (2005).
- [15] T. Baba, Slow light in photonic crystals, *Nat. Photonics* **2**, 465 (2008).
- [16] J. Li, T. P. White, L. O'Faolain, A. Gomez-Iglesias, and T. F. Krauss, Systematic design of flat band slow light in photonic crystal waveguides, *Optics Express* **16**, 6227 (2008).
- [17] T. Ergin, N. Stenger, P. Brenner, J. B. Pendry, and M. Wegener, Three-Dimensional invisibility cloak at optical wavelengths, *Science* **328**, 337 (2010).

- [18] A. Mekis, J. C. Chen, I. Kurland, S. Fan, P. R. Villeneuve, and J. D. Joannopoulos, High Transmission through Sharp Bends in Photonic Crystal Waveguides, *Phys. Rev. Lett.* **77**, 3787 (1996).
- [19] L. Lu, J. D. Joannopoulos, and M. Soljačić, Topological photonics, *Nat. Photonics* **8**, 821 (2014).
- [20] A. B. Khanikaev and G. Shvets, Two-dimensional topological photonics, *Nat. Photonics* **11**, 763 (2017).
- [21] T. Ozawa, H. M. Price, A. Amo, N. Goldman, M. Hafezi, L. Lu, M. C. Rechtsman, D. Schuster, J. Simon, O. Zilberberg, and I. Carusotto, Topological photonics, *Rev. Mod. Phys.* **91**, 015006 (2019).
- [22] Z. Wang, Y. D. Chong, J. D. Joannopoulos, and M. Soljacic, Reflection-Free One-Way Edge Modes in a Gyromagnetic Photonic Crystal, *Phys. Rev. Lett.* **100**, 013905 (2008).
- [23] Z. Wang, Y. Chong, J. D. Joannopoulos, and M. Soljacic, Observation of unidirectional backscattering-immune topological electromagnetic states, *Nature* **461**, 772 (2009).
- [24] Y. Poo, R. X. Wu, Z. Lin, Y. Yang, and C. T. Chan, Experimental Realization of Self-Guiding Unidirectional Electromagnetic Edge States, *Phys. Rev. Lett.* **106**, 093903 (2011).
- [25] M. Hafezi, E. A. Demler, M. D. Lukin, and J. M. Taylor, Robust optical delay lines with topological protection, *Nat. Phys.* **7**, 907 (2011).
- [26] K. Fang, Z. Yu, and S. Fan, Realizing effective magnetic field for photons by controlling the phase of dynamic modulation, *Nat. Photonics* **6**, 782 (2012).
- [27] M. C. Rechtsman, J. M. Zeuner, Y. Plotnik, Y. Lumer, D. Podolsky, F. Dreisow, S. Nolte, M. Segev, and A. Szameit, Photonic floquet topological insulators, *Nature* **496**, 196 (2013).
- [28] A. B. Khanikaev, S. H. Mousavi, W. K. Tse, M. Kargarian, A. H. MacDonald, and G. Shvets, Photonic topological insulators, *Nat. Mater.* **12**, 233 (2013).
- [29] T. Ma and G. Shvets, All-si valley-hall photonic topological insulator, *New J. Phys.* **18**, 025012 (2016).
- [30] J. W. Dong, X. D. Chen, H. Zhu, Y. Wang, and X. Zhang, Valley photonic crystals for control of spin and topology, *Nat. Mater.* **16**, 298 (2017).
- [31] T. Ma and G. Shvets, Scattering-free edge states between heterogeneous photonic topological insulators, *Phys. Rev. B* **95**, 165102 (2017).
- [32] F. Gao, H. Xue, Z. Yang, K. Lai, Y. Yu, X. Lin, Y. Chong, G. Shvets, and B. Zhang, Topologically protected refraction of robust kink states in valley photonic crystals, *Nat. Phys.* **14**, 140 (2017).
- [33] X. Wu, Y. Meng, J. Tian, Y. Huang, H. Xiang, D. Han, and W. Wen, Direct observation of valley-polarized topological edge states in designer surface plasmon crystals, *Nat. Commun.* **8**, 1304 (2017).
- [34] L. Ye, Y. Yang, Z. Hong Hang, C. Qiu, and Z. Liu, Observation of valley-selective microwave transport in photonic crystals, *Appl. Phys. Lett.* **111**, 251107 (2017).
- [35] X. T. He, E. T. Liang, J. J. Yuan, H. Y. Qiu, X. D. Chen, F. L. Zhao, and J. W. Dong, A silicon-on-insulator slab for topological valley transport, *Nat. Commun.* **10**, 872 (2019).
- [36] M. I. Shalaev, W. Walasik, A. Tsukernik, Y. Xu, and N. M. Litchinitser, Robust topologically protected transport in photonic crystals at telecommunication wavelengths, *Nat. Nanotechnol.* **14**, 31 (2019).
- [37] X.-D. Chen, W.-M. Deng, F.-L. Shi, F.-L. Zhao, M. Chen, and J.-W. Dong, Direct Observation of Corner States in Second-Order Topological Photonic Crystal Slabs, *Phys. Rev. Lett.* **122**, 233902 (2019).